TAO data support the existence of large high frequency variations in cross-equatorial overturning circulation

L. E. Baker[1], M. J. Bell[2], A. T. Blaker[3]

[1]Imperial College London, United Kingdom
[2]Met Office, Exeter, United Kingdom
[3]National Oceanography Centre, Southampton, United Kingdom

Key Points:

- Theory and models suggest that internal waves cause large oscillations in the equatorial Pacific meridional overturning circulation (MOC).
- Trapped equatorial waves with similar periods of 3-15 days have previously been observed using a mooring array in the equatorial Pacific.
- We show that there is good agreement between observations and simulations, supporting the large equatorial MOC variability in the models.

Corresponding author: L.E. Baker, l.baker18@imperial.ac.uk

Abstract

Large amplitude oscillations in the meridional overturning circulation (MOC) have been found near the equator in all major ocean basins in the NEMO ocean general circulation model. With periods of 3-15 days and amplitudes of $\sim \pm 100$ Sv in the Pacific, these oscillations have been shown to correspond to zonally integrated equatorially trapped waves forced by winds within 10° N/S of the equator. Observations of dynamic height from the Tropical Atmosphere Ocean (TAO) mooring array in the equatorial Pacific also exhibit spectral peaks consistent with the dispersion relation for equatorially trapped waves. Here, we revisit the TAO observations to confirm that the amplitude of the oscillations is consistent with the simulations, supporting the modelled large amplitude MOC oscillations. We also show that the zonal structure of the frequency spectrum in both observations and simulations is predicted by changes in the baroclinic wave speed with variation in stratification across the ocean basin.

Plain Language Summary

The meridional overturning circulation (MOC) is a large scale oceanic circulation that occurs in each of the main ocean basins and plays an important role in regulating Earth's climate. Global ocean models have shown that large oscillations of the MOC with periods of 3-15 days occur near the equator. These oscillations have been shown to be consistent with basin-scale internal waves, trapped near the equator by the Earth's rotation. However, it is uncertain whether such large oscillations occur in reality. Observations from a mooring array in the equatorial Pacific Ocean have previously been shown to exhibit oscillations at similar frequencies, and to also correspond to these internal waves. In this study, we compare the model with the observations in order to determine whether the oscillations found in the model are realistic. We find that there is remarkable agreement between the modelled and observed waves. This supports the existence of the large scale MOC oscillations, and gives confidence in the global ocean model for representing these processes.

1 Introduction

The large scale oceanic meridional overturning circulation (MOC) fluxes heat from the tropics to the poles and transports tracers between the surface and abyssal ocean on timescales of hundreds of years. Although the simplified view of the MOC as a slow and steady 'great oceanic conveyor belt' abounds, in practice it exhibits variability on a wide range of timescales (Hirschi et al., 2020). In particular, a range of models show significant MOC variability on the timescale of days near the equator in all main ocean basins (Hirschi et al., 2013, 2020). Whereas over most latitudes the high frequency variability has a standard deviation of a few Sverdrups, near the equator the variability can be very large, up to $\sim \pm 100$ Sv in the Pacific.

Although it remains unknown whether, or to what extent, there is a connection between this variability and the mean transport, the equatorial Pacific MOC is important for a number of reasons. It is thought to interact with the El Nino Southern Oscillation (ENSO) and Pacific Decadal Oscillation (PDO), thus impacting the ventilation of CO_2 in the region (McPhaden & Zhang, 2002; Gruber et al., 2009; Song et al., 2018). High frequency motions also suggest the potential for diapycnal mixing, with implications for the large scale stratification and MOC structure. Recent studies have proposed that equatorial inertia-gravity waves generate significant abyssal mixing (Holmes et al., 2016; Delorme & Thomas, 2019). Equally, it has also been suggested that the strong cross-isopycnal component of inertia-gravity waves may cause spurious diapycnal mixing in models (Griffies et al., 2000; Megann, 2018).

Spectral peaks in sea-level variations at frequencies of 3-5 days were first observed in the Pacific and shown to correspond to equatorially trapped inertia-gravity waves by Wunsch and Gill (1976). The existence and physics of these wind-forced waves is now well known (e.g., Gill, 1982; McCreary, 1985), and many other studies have since confirmed the existence of inertia-gravity (Poincaré) and mixed Rossby-gravity (Yanai) waves in all main ocean basins (e.g., Weisberg & Hayes, 1995; Eriksen, 1980; Garzoli & Katz, 1981; Gilbert & Mitchum, 2001). In particular, Farrar and Durland (2012) (hereafter FD12) used the extensive TAO/TRITON (Triangle Trans-Ocean Buoy Network) mooring record in the equatorial Pacific to identify many Yanai and Poincaré wave modes at periods of 3-15 days. Together with a companion study (Durland & Farrar, 2012), FD12 explained the observed spectral peaks in frequency and zonal wavenumber based on the corresponding observed wind stress spectrum.

A recent two-part study by Blaker et al. (2021) (hereafter B1) and Bell et al. (2021) (hereafter B2) showed that large amplitude oscillations of the MOC found in an integration of the NEMO (Nucleus for European Modelling of the Ocean) global ocean model could be attributed to equatorially trapped Yanai and Poincaré waves driven by winds within $\pm 10^{\circ}$ of the equator. Using idealised simulations based on a zonally averaged formulation of the linear wave theory with zonal boundary conditions of no normal flow, they accurately reproduced the MOC oscillations in the realistic model with a small number of low-mode waves, thus explaining the modelled MOC variability on 3-15 day timescales. The 10 day Yanai and 4 day Poincaré modes were shown to give the largest contributions to the equatorial MOC oscillations. However, the question remains as to whether such large oscillations occur in reality.

In this study, we compare output from the global ocean simulations of B1,2 with the TAO mooring record to verify that zonally integrated fluctuations in dynamic height are consistent with those inferred from the TAO mooring observation data. An early indication of this is the good correspondence between high frequency, zonally averaged dynamic heights from NEMO and TAO data at the equator, plotted for the same time period in figure 1a.

Although the moorings are relatively sparse in latitude and longitude, FD12 showed that it is possible to estimate the temporal and zonal spectrum of dynamic height using least squares methods, finding that most of the power was concentrated at low zonal wavenumbers. Motivated by this and the findings of B1,2 that the zonally averaged effect of these waves could have important consequences for variability of the MOC, we focus on zero zonal wavenumber modes and use similar methods to FD12 to fit the high frequency dynamic height data to a Fourier basis in time and a basis of theoretically-derived meridional modes in latitude. We first compare the temporal/meridional spectra of zonally averaged dynamic height in the model and observations, and show that they are largely consistent with each other and with linear theory. We then explain the zonal structure of the dynamic height power spectrum in terms of the east-west variation in stratification.

2 Equatorial Modes

Equatorially trapped waves can be modelled as linear perturbations upon a base state with zero background current and a background stratification $N(z)$. The solution for unforced waves on a beta plane can be found from the hydrostatic, incompressible, linear, unforced and inviscid momentum and buoyancy equations (Wunsch & Gill, 1976; Durland & Farrar, 2012; Bell et al., 2021). The meridional velocity is given by:

$$v(x,y,z,t) = \sum_{m,n} \left[p_m(z)\phi_{m,n}(y) \int_{-\infty}^{\infty} V_{m,n}(k) e^{i(kx-\omega_{m,n}(k)t)}\, dk \right] \tag{1}$$

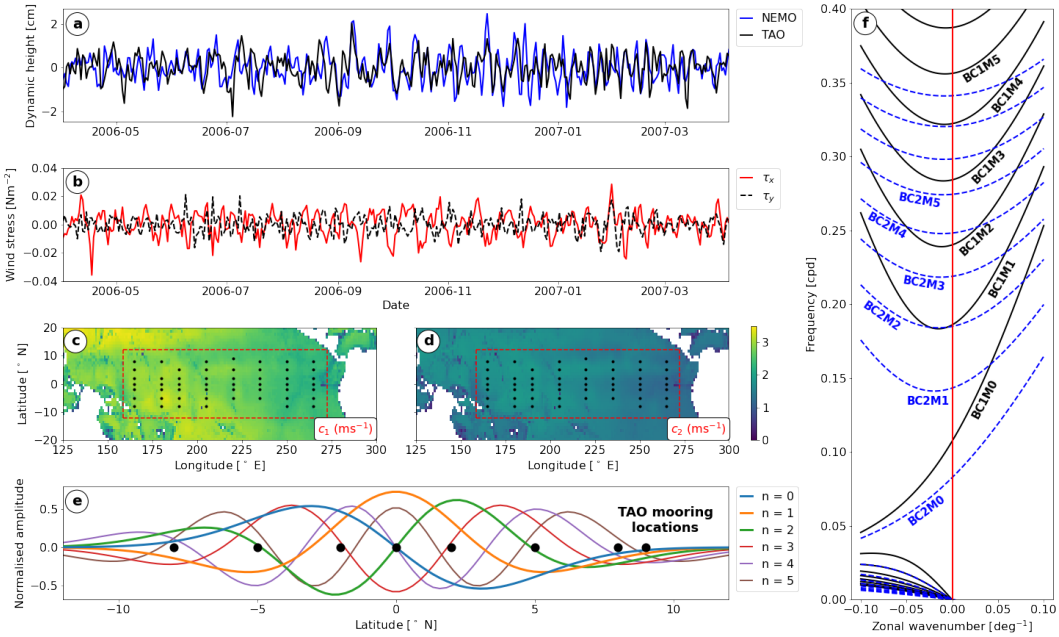

Figure 1. (a) High-pass filtered and zonally averaged 500 dbar dynamic height at the equator for sampled NEMO data (blue) and TAO mooring data (black). (b) High-pass filtered and zonally averaged zonal (τ_x) and meridional (τ_y) wind stress at the equator used to force the NEMO simulation.(c) c_1 and (d) c_2, calculated from WOCE neutral density data. The red dashed box shows the subdomain of the global NEMO simulation used, and black circles show locations of TAO moorings. (e) Meridional structure of pressure modes for baroclinic mode 1, $c_1 = 2.7\,\mathrm{m\,s^{-1}}$, $k = 0$. TAO mooring latitudes shown as black circles. (f) Dispersion relation for unforced equatorial modes. The first (second) baroclinic modes are shown in black (blue dashed), for baroclinic wave speeds $c_1 = 2.7\,\mathrm{m\,s^{-1}}$ and $c_2 = 1.6\,\mathrm{m\,s^{-1}}$ (their values averaged over the red dashed subdomain in (c,d)). The red line shows $k = 0$, and the labelling convention is such that 'BC2M1' corresponds to baroclinic mode 2, meridional mode 1.

where $p_m(z)$ are a set of vertical modes and $\phi_{m,n}(y)$ is the nth meridional mode for the mth baroclinic mode. Full expressions are given in Appendix A (A1) - (A3). The frequency $\omega_{m,n}$ and zonal wavenumber k satisfy the dispersion relation:

$$\left(\omega_{m,n}^2/c_m^2 - k^2 - k\beta/\omega_{m,n}\right)\frac{c_m}{2\beta} = n + \frac{1}{2} \tag{2}$$

where c_m is the mth baroclinic wave speed (see Appendix A, (A1)), β is the Rossby parameter, and $V_{m,n}(k)$ determines the zonal wavenumber content of each vertical/meridional mode combination. In an unforced and undamped scenario, $V_{m,n}(k)$ would be set by the initial conditions. However, in reality and in the model the waves are both forced by surface winds and damped by turbulent processes (parameterised in the model). Durland and Farrar (2012) derived the relationship between the wind forcing and the resulting wave field, and B1,2 showed using a global ocean model and idealised simulations that wind forcing between $\pm 10°$N is essential to the generation of the resulting MOC fluctuations. The effect of the wind forcing is to resonantly excite particular components of the free wave solution, dependent on the spatial structure and frequency content of the winds. We therefore expect to find waves corresponding to the unforced solutions (1) in the forced ocean.

Figure 1f shows the dispersion relation (2) for $n = 0, 1, 2, 3, 4, 5$, $m = 1, 2$. The notation used is the same as that of FD12: 'BC m' refers to the mth baroclinic mode, and 'M n' refers to the nth meridional mode. The curves in the lower left are Rossby waves, and the dispersion relations $\omega = c_m k$ for Kelvin waves are not shown, since we are interested in long zonal wavelengths and high frequencies. The $n \geq 1$ waves are Poincaré waves, and the $n = 0$ waves are Yanai waves. FD12 found spectral peaks in the TAO dynamic height record of long zonal wavelength ($k \simeq 0$) waves agreeing well with these dispersion relations.

We estimate the meridional spectrum of the waves by fitting to theoretical meridional modes, rather than a standard Fourier basis. Since dynamic height is proportional to pressure, instead of using the meridional velocity modes $\phi_{m,n}(y)$, we find the corresponding modes for pressure as in Durland and Farrar (2012), using $k = 0$.

The first baroclinic mode is expected to be dominant, and we therefore fit to meridional modes with $m = 1$, although we will demonstrate that our choice of meridional modes still allows detection of the baroclinic mode 2. The baroclinic wave speeds c_1 and c_2 in the Pacific are shown in figure 1 c,d. These were calculated from the vertical eigenvalue equation (A1) using Galerkin methods and gridded neutral density data from the World Ocean Circulation Experiment (WOCE) atlas (Gouretski & Koltermann, 2004), and c_1 was verified against a similar calculation by Chelton et al. (1998).

Figure 1e shows the first 6 normalised meridional modes for pressure for the baroclinic mode 1 when $k = 0$. The black circles show the meridional locations of the TAO moorings, although in practise the meridional TAO data is much more sparse due to missing data and no moorings at some longitudes. This limits our ability to properly resolve the meridional structure, and it was concluded by FD12 that this resolution was insufficient to project the TAO data onto meridional modes - they instead focused on symmetry/antisymmetry about the equator. However, we demonstrate some success in using the TAO moorings to uncover the meridional structure of the waves.

3 Data

3.1 TAO data

We use 26 years of data (1st Jan 1993 - 31st Dec 2018) from the TAO mooring array, with locations spanning the equatorial Pacific (figure 1c,d). Daily averages of surface dynamic height relative to 500 dbar are used throughout; the dataset is described

in detail in FD12. We exclude some TAO and nearby TRITON moorings on the western side of the array (not shown in figure 1c,d), since there isn't coverage both sides of the equator at these longitudes. For 'like-for-like' comparison with the year-long NEMO output, we take the corresponding year (1 April 2006 - 5 April 2007) in the TAO timeseries, labelled in plots as 'TAO: sampled'. When the full timeseries is used, it is labelled 'TAO: full data'.

3.2 NEMO simulation

We use the NEMO v3.2 global ocean model at 1/4° horizontal resolution (Madec, 2008). The configuration is the control simulation described in B1, and we take one year of data from 1 April 2006 - 5 April 2007. We use daily average fields of surface dynamic height relative to 500 dbar for consistency with the TAO dataset, and the spatial domain is bounded zonally to contain the most western and eastern TAO moorings, and meridionally by ±12°N, shown as the red dashed box in figures 1c,d. The model is forced using the CORE2 IAF dataset (Large & Yeager, 2009), with wind stress based on the NCEP reanalysis (Kalnay et al., 1996), thus winds forcing the model are intended to represent the true wind field for the same time period.

For 'like-for-like' comparison with the TAO dataset, we sample the NEMO output at the locations of the TAO moorings, and remove data that are missing in the corresponding TAO timeseries. These data are labelled in plots as 'NEMO: sampled', and the full spatial data are labelled as 'NEMO: full data'.

4 Methods

To estimate the power spectra of the dynamic height fields in NEMO and TAO, we follow FD12 and use a least squares fitting method. FD12 fitted in time and longitude; we instead fit in time and latitude. If there were no missing data, the temporal fit could be accomplished using a discrete Fourier transform, but given the nature of the mooring data a least squares fit to Fourier modes in time is more appropriate and allows us to use all of the data. This also has the advantage of allowing us to fit in latitude to the theoretical meridional basis of pressure modes explained in §2.

4.1 Least squares fit

We use a tapered least squares method, described in detail in FD12. The general method can be explained for 1D data; 2D (time and space) data are first flattened to one dimension. First, L modes are chosen as a basis for the data $\mathbf{h}$ of size N, and stored in a matrix $\mathbf{E}$ of size $N \times L$. The model can then be written as

$$\mathbf{h} = \mathbf{E}\mathbf{x} + \mathbf{n} \tag{3}$$

where $\mathbf{x}$ (size M) contains the coefficients of the modes, and $\mathbf{n}$ (size N) is the noise in the data. The tapered least squares solution for $\mathbf{x}$ minimises the sum of squares

$$J = \frac{\mathbf{n}^T\mathbf{n}}{\sigma_n^2} + \frac{\mathbf{x}^T\mathbf{x}}{\Delta_x^2} \tag{4}$$

and is given by:

$$\mathbf{x} = \left(\mathbf{E}^T\mathbf{E} + r\mathbf{I}\right)^{-1}\mathbf{E}^T\mathbf{h} \tag{5}$$

where the parameter $r = \sigma_n^2/\Delta_x^2$ is the 'noise to signal ratio', with σ_n^2 the expected variance in the noise, and Δ_x^2 the expected variance in the coefficients of the model.

4.2 Temporal modes

The temporal extent of the NEMO and sampled TAO datasets is 370 days. We define a full set of 185 frequencies equally spaced between $\omega_{min} = 1/370$ cpd and $\omega_{max} =$

1/2 cpd with a resolution of ω_{min}. We then create a full set of 370 temporal modes consisting of a sine and cosine at each of these frequencies.

The full 26 year TAO time series is split into non-overlapping periods of 370 days, and the resulting spectrum for each is averaged to give the 'TAO: full' spectrum. The temporal modes are thus the same as for the other datasets, allowing comparison to spectra of the shorter time series whilst providing a more reliable estimate.

4.3 Meridional modes

The meridional modes are found from the theoretical solution for the baroclinic mode 1 (A2), converted for pressure at $k = 0$. We use the first 6 modes, as we find that this gives the best balance between representing the higher mode wave signals present in the data and minimising overfitting associated with too many model parameters.

4.4 Fitting procedure

Before performing the least squares fit, we apply a high pass filter at 20 days (0.05 cpd) to remove any low frequency Rossby waves (see figure 1f) and other non-wavelike structures. The method is described in detail in Appendix B. This step is particularly important when zonally averaging the TAO data, as the average can easily be contaminated by missing data coming into/out of the record.

We then find the temporal/meridional power spectrum both for zonally averaged fields (e.g. figure 2) and at each longitude separately (e.g. figure 3). When taking a zonal average, we remove any times/latitudes with data at only a single longitude. The set of temporal frequencies is truncated to those higher than 0.05 cpd, since those below this have already been removed in the high pass filter, leaving 167 of the 185 original frequencies. The $167 \times 2 = 334$ temporal and 6 meridional modes are cross-multiplied and flattened to give a set of $334 \times 6 = 2004$ modes, and these form the matrix $\mathbf{E}$. The noise to signal ratio r is taken to be 35; see Appendix C for justification.

The coefficients $\mathbf{x}$ of the modes are then estimated using (5). There are two modes at each frequency and meridional mode number, corresponding to the temporal sine and cosine. The power is then defined as the square root of the sum of these two coefficients squared.

5 Results

We first directly compare the model data to the observations. Figure 1a shows the high pass filtered (see Appendix B) and zonally averaged 500 dbar dynamic height in NEMO and TAO at the equator, both sampled for a 'like-for-like' comparison. The similarity between the fields is remarkable - the peaks and troughs often agree well, showing that the model captures much of the varying phase and amplitude of the variations. Although the ocean model is forced by realistic winds, this level of agreement is somewhat surprising and lends credence to the idea of wave excitation being deterministic rather than stochastic. Agreement at longer timescales and higher latitudes (not shown) is also good. Figure 1b confirms that there is no obvious relationship between the amplitudes of the meridional and zonal wind stress and the dynamic height; see Durland and Farrar (2012) for a derivation of the complex dependence of wave amplitudes on wind stresses.

Note that although the dynamic height time series does not appear to agree with that of the MOC streamfunction at the equator from NEMO shown in B1, (their figure 4a), this is expected since meridional velocity modes have opposite symmetry about the equator to those of dynamic height. The time series of dynamic height at the equator does not contain a contribution from the 10 day ($n = 0$) mode since the correspond-

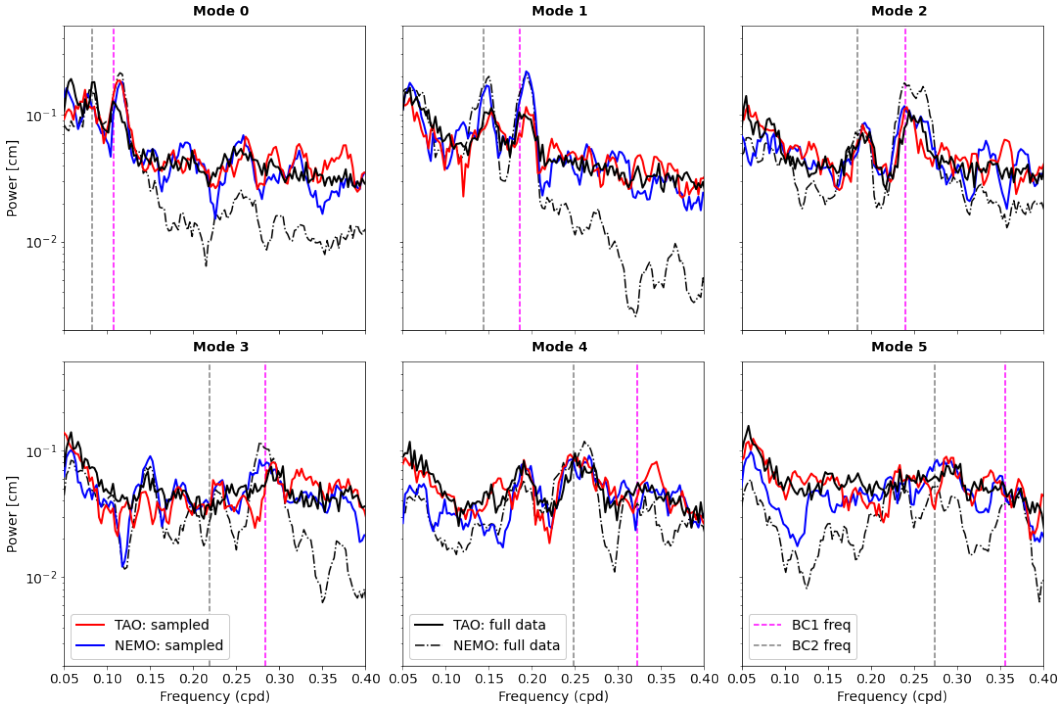

Figure 2. Temporal and meridional spectrum of zonally averaged 500 dbar dynamic height. Each panel shows a meridional mode, and a rolling mean over 5 frequencies is shown. Red shows TAO data for the duration of the NEMO simulation, blue shows NEMO data sampled at locations and times of available TAO data. Black dot-dashed shows NEMO data with full spatial resolution, and black solid shows TAO data from the full 26 year timeseries. Magenta (grey) dashed lines show the predicted $k = 0$ frequency of the baroclinic mode 1 (mode 2), calculated using the dispersion relation (2) and the baroclinic wavespeeds shown in figures 1c,d, averaged over red-dashed NEMO subdomain.

ing pressure mode is zero at the equator (see figures 1e,f), whereas the 10 day mode is contained (and at times dominant) in the time series of the MOC streamfunction (B1,2) since the $n = 0$ mode for meridional velocity has a maximum at the equator. Furthermore, the MOC time series (B1,2) is at 1583 m depth, whereas the 500 dbar dynamic height is calculated by integrating the specific volume anomaly over the top 500 m of the ocean, and is thus more representative of upper ocean dynamics and wave structures.

Figure 2 shows the temporal/meridional spectra of the zonally averaged dynamic height data. The black dot-dashed line showing the spectrum of the full NEMO simulation exhibits well defined peaks at (or just above) the expected frequencies, particularly for the first 3 meridional modes. There are also peaks in each spectrum corresponding to other meridional modes of the same symmetry - this indicates an imperfect fit of the basis functions to the data, and is expected (for example, we are using a baroclinic mode 1, $k = 0$ meridional basis to represent all baroclinic modes). Due to the completeness and high spatial resolution of this dataset, there is less power at the higher frequencies than in the other datasets, which predictably pick up more 'noise', due to both the limited meridional resolution and the missing data in the zonal average.

The blue line shows the sampled NEMO data, and this should be compared to the red sampled TAO data for a 'like-for-like' comparison between the model and observations. Both exhibit peaks at the predicted frequencies (using $k = 0$ in (2)) for at least

the first 4 modes, and they show excellent similarity at most frequencies and meridional modes. In particular, they have identical peaks at both the baroclinic modes in the meridional modes 0,2 and 3. There is a discrepancy of a factor of ~ 2 in the amplitude of the BC1M1 and BC2M1 peaks between the TAO and NEMO data, which is consistent between both their respective 'full' and 'sampled' datasets, suggesting that this is a true difference between the model and observations.

Overall, the comparison of the zonally averaged fields shows that the modelled large amplitude oscillations of the Pacific MOC found by Blaker et al. (2021); Bell et al. (2021) are largely consistent with observed amplitudes, although NEMO appears to overpredict the amplitude of the BC1M1 and BC2M1 modes by a factor of two. The comparison between the full spatial and spatially sampled datasets allows us to evaluate the usefulness of the TAO mooring array in representing these waves over the full equatorial ocean. Although the spectrum calculated using the full data (black dashed) deviates from the sampled data (blue lines) somewhat at higher frequencies, the agreement at lower frequencies and at many of the spectral peaks is very good. The TAO mooring array therefore provides a good view of the large scale wave field.

Next, we perform the least squares fit at each longitude. Figure 3 shows the resulting spectra for the same four datasets as figure 2. The predicted frequencies are now plotted as a function of longitude, and show a decrease in frequency from west to east. This is due to a decrease in stratification across the Pacific causing a decrease in baroclinic wave speed (c.f. figures 3b,c) and is also evident in each of the spectra, where there is again very good correspondence between the predicted and modelled/observed peak frequencies. There is a slight underprediction of each frequency for higher meridional modes. This could be due to biases in the sensitive calculation of wave speed (Chelton et al., 1998), or due to non-zero zonal wavenumber in the observed waves - the dispersion relations plotted in figure 1f show that frequencies increase away from the near $k = 0$ minima.

The middle two rows give the 'like for like' comparison, and as in figure 2, there is very good agreement between observations and model. It is once again clear that the meridional mode 1 amplitudes are higher in the model than in observations. Peak amplitudes in the full TAO spectrum are in general slightly lower, consistent with figure 2, although there is also a corresponding reduction in the noise in the full TAO spectrum compared with the one year spectrum. The 10 day BC1M0 peak in the full TAO data has significant variation on 1-2 year timescales, with one significant peak occurring in the duration of the NEMO simulation (not shown), explaining why the sampled TAO peak is higher than the full TAO peak at the BC1M0 frequency in figure 2.

6 Conclusions

In this study, we have narrowed the gap between realistic numerical simulations (B1,2) and observations (FD12) of equatorially trapped Yanai and Poincaré waves. We have shown that the wave fields examined by each set of authors are largely consistent with each other and with linear theory in terms of amplitude, frequency and meridional structure, both in the zonal average and in terms of their east-west variation. In particular, there is very good agreement between the observed and modelled amplitudes of the 10 day BC1M0 mode shown by B1,2 to be leading order in the equatorial MOC variability. This observationally verifies the explanation of the equatorial MOC variability on 3-15 day timescales of B1,2, and validates the skill of the NEMO ocean model in reproducing the leading equatorial Poincaré and Yanai waves, although there appears to be overprediction in NEMO by a factor of two of Poincaré waves of period 5-7 days.

The success of the NEMO ocean model in modelling these waves gives confidence in this and other similar global ocean models for modelling the equatorial MOC, which itself has an important role in the climate system through phenomena such as the ENSO

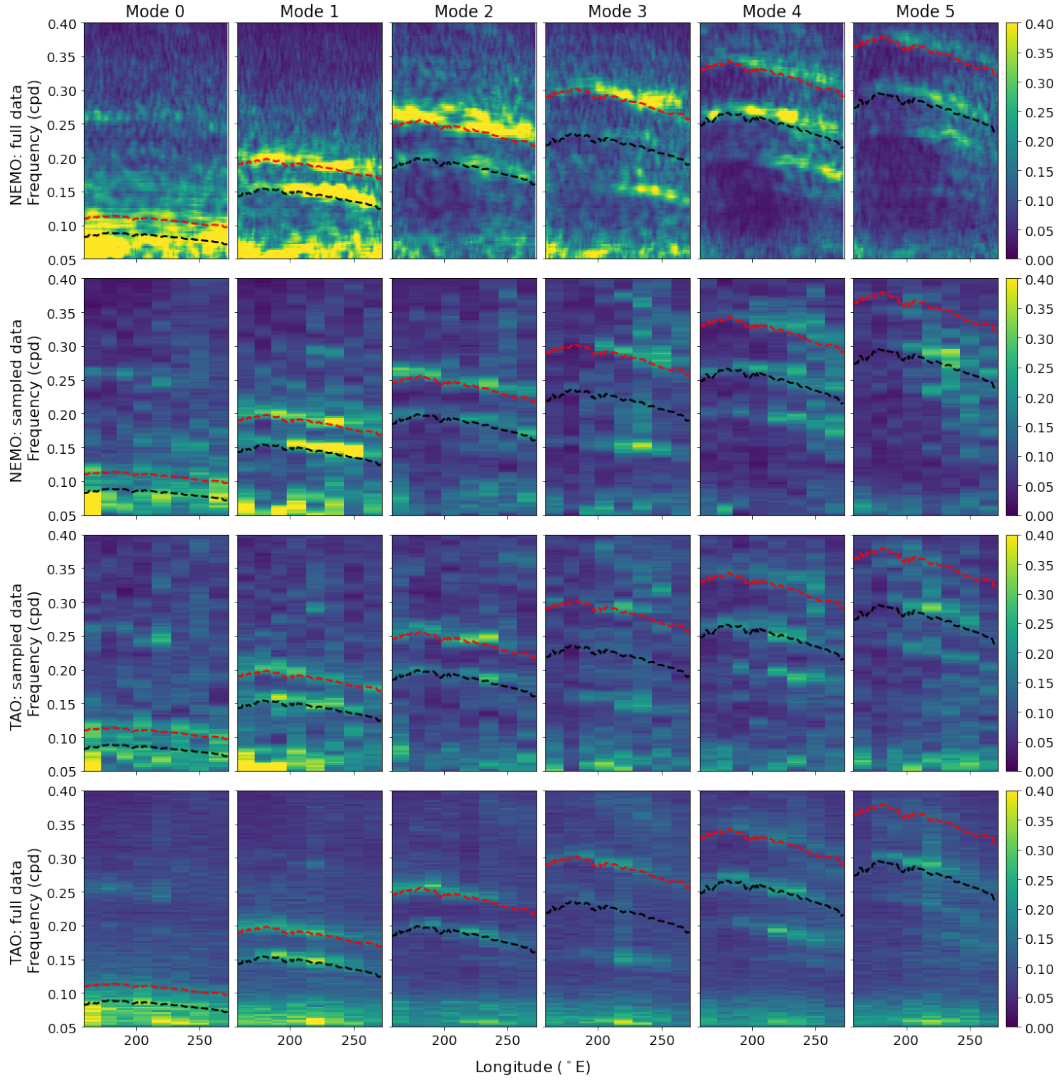

Figure 3. Zonal structure of dynamic height power spectrum, split in columns by meridional mode. (Top) NEMO dataset with full spatial resolution, (upper middle) NEMO dataset sampled at TAO locations and times, (lower middle) TAO dataset for the duration of the NEMO simulation, and (bottom) full TAO dataset. The top 3 rows show a rolling mean over 5 frequencies, and the bottom row is calculated as an average over spectra of one year moving windows. Red (black) dashed lines show the predicted baroclinic mode 1 (mode 2) frequencies of equatorial modes, using the baroclinic wave speeds at the equator shown in figure 1c,d.

and PDO (McPhaden & Zhang, 2002). The strong dependence of the trapped equatorial waves on wind forcing (B1,2, Durland & Farrar, 2012) raises questions about their role in fluxing energy and momentum into the interior ocean. In particular, if equatorial inertial-gravity waves have a significant impact on diapycnal mixing and upwelling as suggested by Holmes et al. (2016); Delorme and Thomas (2019), their representation and the parameterisation of related unresolved turbulent processes in climate models will be important.

Appendix A Equatorial mode equations

The structure of the equatorial modes is given by (1) in the main text. $p_m(z)$, $m \geq 1$, are a set of vertical modes, and c_m the mth baroclinic wave speed, found by solving the eigenvalue problem:

$$\frac{\partial}{\partial z}\left(\frac{1}{N^2}\frac{\partial p_m}{\partial z}\right) + \frac{p_m}{c_m^2} = 0\,, \qquad \frac{\partial p_m}{\partial z} = 0,\ z = 0,\, H \tag{A1}$$

The nth meridional mode $\phi_{m,n}(y)$ for the mth baroclinic mode $p_m(z)$ is given by

$$\phi_{m,n}(y) = e^{-\tilde{y}_m^2/4} He_n(\tilde{y}_m) \tag{A2}$$

$$\tilde{y}_m = \left(\frac{2\beta}{c_m}\right)^{\frac{1}{2}} y \tag{A3}$$

where He_n is the nth Hermite polynomial, and β is the Rossby parameter. The frequency $\omega_{m,n}$ and zonal wavenumber k satisfy the dispersion relation (2) in the main text.

Appendix B High pass filter

We perform a high pass filter at 20 days before zonally averaging or fitting the dynamic height data. First, we remove a rolling mean of length 21 days at each location - this is necessary to avoid spurious effects at the endpoints of the timeseries and gaps in the data. This alone isn't sufficient to remove the lower frequency signals, so we then perform a fit in time only at each location using the least squares method (§4.1) and the full set of temporal modes (§4.2). A low-pass fit consisting of the reconstructed field from frequencies lower than 0.05 cpd is then subtracted from the original field to give a high pass filtered dynamic height at each location.

Appendix C Choice of noise to signal ratio

The parameter $r = \sigma_n^2/\Delta_x^2$ must be small enough to capture the 'true' variance of the data, but large enough to avoid overfitting to the 'noise'. We found high sensitivity of results to r due to the missing mooring data and the large number of parameters in our model. FD12 estimated the noise standard deviation σ_n to be 0.5 cm, and used Parseval's relation to estimate the model variance Δ_x^2 from the data variance. Our meridional pressure modes are not orthogonal (although the meridional velocity modes $\phi_{m,n}(y)$ are), so instead we use the spatially resolved NEMO dataset to choose an appropriate value of r as follows.

First, we fit the 2004-parameter model to the full NEMO dataset. The number of datapoints here is over 18 times the number of model parameters, significantly reducing the risk of overfitting. For very small r (forcing the 'best' fit possible, in terms of the lowest model-data error) the model can represent 79% of the variance of the data. We then choose $r = 35$, which in the full NEMO dataset allows the model to represent 95% of the variance of the 'best fit' (itself representing 79% of the data variance). This is true of both the fit to the zonal average and at individual longitudes. With $r = 35$ and Δ_x^2 given by the actual variance of the model, the corresponding value of σ_n for the fit is $\sim$

0.2 cm for the zonal average and ~ 0.8 cm at individual longitudes, similar to the estimate of FD12 of 0.5 cm for the noise variance.

Acknowledgments

LB was supported by the Centre for Doctoral Training in Mathematics of Planet Earth, UK EPSRC funded (grant no. EP/L016613/1). MJB was supported by the Met Office Hadley Centre Climate Programme funded by BEIS. ATB acknowledges support from the NERC projects CLASS (NE/R015953/1) and MESO-CLIP (NE/K005928/1). The authors are grateful for helpful comments from Joël Hirschi, and thank the GTMBA Project Office of NOAA/PMEL for providing the TAO dynamic height data.

The TAO mooring data is available at https://www.pmel.noaa.gov/tao/drupal/disdel/. The NEMO simulation data and code required to enable the reader to reproduce our results are available online at https://doi.org/10.5281/zenodo.5637010 (Baker et al., 2021).

References

Baker, L., Bell, M. J., & Blaker, A. (2021). *TAO data support the existence of large high frequency variations in cross-equatorial overturning circulation: software and data.* Zenodo. doi: 10.5281/zenodo.5637010

Bell, M. J., Blaker, A. T., & Hirschi, J. J.-M. (2021). Wind-Driven Oscillations in Meridional Overturning Circulations near the Equator. Part II: Idealized Simulations. *J. Phys. Oceanogr.*, *51*(3), 663–683. doi: 10.1175/jpo-d-19-0297.1

Blaker, A. T., Hirschi, J. J.-M., Bell, M. J., & Bokota, A. (2021). Wind-Driven Oscillations in the Meridional Overturning Circulation near the equator. Part I: Numerical Models. *J. Phys. Oceanogr.*, *51*(3), 645–661. doi: 10.1175/jpo-d-19-0296.1

Chelton, D. B., Deszoeke, R. A., Schlax, M. G., El Naggar, K., & Siwertz, N. (1998). Geographical variability of the first baroclinic Rossby radius of deformation. *J. Phys. Oceanogr.*, *28*(3), 433–460.

Delorme, B. L., & Thomas, L. N. (2019). Abyssal mixing through critical reflection of equatorially trapped waves off smooth topography. *J. Phys. Oceanogr.*, *49*(2), 519–542. doi: 10.1175/JPO-D-18-0197.1

Durland, T. S., & Farrar, J. T. (2012). The wavenumber-frequency content of resonantly excited equatorial waves. *J. Phys. Oceanogr.*, *42*(11), 1834–1858. doi: 10.1175/JPO-D-11-0234.1

Eriksen, C. C. (1980). Evidence for a continuous spectrum of equatorial waves in the Indian Ocean. *J. Geophys. Res.*, *85*(C6), 3285. doi: 10.1029/jc085ic06p03285

Farrar, J. T., & Durland, T. S. (2012). Wavenumber-frequency spectra of inertia-gravity and mixed Rossby-gravity waves in the equatorial Pacific Ocean. *J. Phys. Oceanogr.*, *42*(11), 1859–1881. doi: 10.1175/JPO-D-11-0235.1

Garzoli, S., & Katz, E. J. (1981). Observations of Inertia-Gravity Waves in the Atlantic from Inverted Echo Sounders during FGGE. *J. Phys. Oceanogr.*, *11*, 1463–1473.

Gilbert, S., & Mitchum, G. (2001). Equatorial Inertia - gravity Waves Observed in TOPEX / Poseidon Sea Surface Heights waves observed in TOPEX / Poseidon sea surface heights. *Geophys. Res. Lett.*, *28*(12), 2465–2468.

Gill, A. E. (1982). *Atmosphere–Ocean Dynamics.*

Gouretski, V. V., & Koltermann, K. P. (2004). WOCE Global Hydrograhic Climatology. *Berichte des BSH, 35, Bundesamt für Seeschiffsfahrt und Hydrogr. Hambg.*(35/2004).

Griffies, S. M., Pacanowski, R. C., & Hallberg, R. W. (2000). Spurious diapycnal mixing associated with advection in a z-coordinate ocean model. *Mon. Weather Rev.*, *128*(3), 538–564. doi: 10.1175/1520-0493(2000)128⟨0538:SDMAWA⟩2.0.CO;2

Gruber, N., Gloor, M., Mikaloff Fletcher, S. E., Doney, S. C., Dutkiewicz, S., Follows, M. J., ... Takahashi, T. (2009). Oceanic sources, sinks, and transport of atmospheric CO2. *Global Biogeochem. Cycles*, *23*(1), 1–21. doi: 10.1029/2008GB003349

Hirschi, J. J., Barnier, B., Böning, C., Biastoch, A., Blaker, A. T., Coward, A., ... Xu, X. (2020). The Atlantic Meridional Overturning Circulation in High-Resolution Models. *J. Geophys. Res. Ocean.*, *125*(4), 1–35. doi: 10.1029/2019JC015522

Hirschi, J. J., Blaker, A. T., Sinha, B., Coward, A., De Cuevas, B., Alderson, S., & Madec, G. (2013). Chaotic variability of the meridional overturning circulation on subannual to interannual timescales. *Ocean Sci.*, *9*(5), 805–823. doi: 10.5194/os-9-805-2013

Holmes, R. M., Moum, J. N., & Thomas, L. N. (2016). Evidence for seafloor-intensified mixing by surface-generated equatorial waves. *Geophys. Res. Lett.*, *43*(3), 1202–1210. doi: 10.1002/2015GL066472

Kalnay, E., Kanamitsu, M., Kistler, R., Collins, W., Deaven, D., & Gandin, L. (1996). The NCEP / NCAR 40-Year Reanalysis Project. *Bull. Am. Meteorol. Soc.*, *77*(3), 437–471.

Large, W. G., & Yeager, S. G. (2009). The global climatology of an interannually varying air - Sea flux data set. *Clim. Dyn.*, *33*(2-3), 341–364. doi: 10.1007/s00382-008-0441-3

Madec, G. (2008). NEMO ocean engine. *Note du Pole modélisation 27, Inst. Pierre-Simon Laplace*, 209pp.

McCreary, J. (1985). Modeling Equatorial Ocean Circulation. *Annu. Rev. Fluid Mech.*(17), 359–409.

McPhaden, M. J., & Zhang, D. (2002). Slowdown of the meridional overturning circulation in the upper Pacific Ocean. *Nature*, *415*(6872), 603–608. doi: 10.1038/415603a

Megann, A. (2018). Estimating the numerical diapycnal mixing in an eddy-permitting ocean model. *Ocean Model.*, *121*(November 2017), 19–33. doi: 10.1016/j.ocemod.2017.11.001

Song, L., Li, Y., Wang, J., Wang, F., Hu, S., Liu, C., ... Guan, C. (2018). Tropical Meridional Overturning Circulation Observed by Subsurface Moorings in the Western Pacific. *Sci. Rep.*, *8*(1), 1–8. doi: 10.1038/s41598-018-26047-7

Weisberg, R. H., & Hayes, S. P. (1995). Upper ocean variability on the equator in the Pacific at 170°W. *J. Geophys. Res. Ocean.*, *100*(C10), 20,485–20,498. doi: 10.1029/95JC01886

Wunsch, C., & Gill, A. E. (1976). Observations of equatorially trapped waves in Pacific sea level variations. *Deep. Res. Oceanogr. Abstr.*, *23*(5), 371–390. doi: 10.1016/0011-7471(76)90835-4